A novel 3D plasmonic p-n heterojunction photocatalyst: Ag nanoparticles on flower-like p-Ag$_2$S/n-BiVO$_4$ and its excellent photocatalytic reduction and oxidation activities

Zhao Wei[a,b,c], Dai Benlin[a], Zhu Fengxia[a], Tu Xinyue[a], Xu Jiming[a,*], Zhang Lili[a,*], Li Shiyin[c], Dennis Y.C. Leung[b,*], Cheng Sun[d]

[a] *Jiangsu Key Laboratory for Biomass-Based Energy and Enzyme Technology, Jiangsu Collaborative Innovation Center of Regional Modern Agriculture & Environmental Protection, School of Chemistry and Chemical Engineering, Huaiyin Normal University, Huaian, PR China*
[b] *Department of Mechanical Engineering, University of Hong Kong, Pokfulam Road, Hong Kong*
[c] *School of Environment, Jiangsu Center for Collaborative Innovation in Geographical Information Resource Development and Application, Nanjing Normal University, Nanjing, PR China*
[d] *State Key Laboratory of Pollution Control and Resource Reuse, School of the Environment, Nanjing University, Nanjing, PR China*

ARTICLE INFO

ABSTRACT

A novel 3D structure Ag/p-Ag$_2$S/n-BiVO$_4$ plasmonic p-n heterojunction photocatalyst was successfully fabricated via a depositing p-type Ag$_2$S on n-type BiVO$_4$, followed by light reduction. In this innovative plasmonic p-n heterojunction photocatalyst strcture, p-n heterojunction can play the role of suppression of charge recombination, and surface plasmon resonance of Ag can enhance the absorption of visible light confirmed by finite difference time domain (FDTD) simulations method. For the photocatalytic oxidation of oxytetracycline hydrochloride (OTH) and reduction of Cr^{6+}, the Ag/p-Ag$_2$S/n-BiVO$_4$exhibits excellent photocatalytic performance, compared with BiVO$_4$ and p-Ag$_2$S/n-BiVO$_4$. The results of active species detection reveal that h$^+$ radical is the main reactive species in the photocatalytic oxidation of OTH. Moreover, 13 photocatalytic degradation intermediates and products of OTH were also identified by the gas chromatography-mass spectrometer (GC-MS). Finally, the photocatalytic oxidation and reduction mechanism over Ag/p-Ag$_2$S/n-BiVO$_4$ was discussed in detail. The present study will benefit the development of the new plasmonic p-n heterojunction photocatalysts and would be of great importance to meet ever-increasing environmental demands in the future.

1. Introduction

Photocatalysis has been regarded as one of the promising technologies for solar energy conversion and the elimination of organic pollutants [1–9]. TiO$_2$, a traditional photocatalyst, has been widely researched due to its excellent optical and electronic properties, low cost, nontoxicity and relatively high chemical stability [10–19]. However, TiO$_2$ with its relatively wide band gap (3.2 eV) limits its practical applications because it only responds to UV irradiation that only constitutes about 4% of solar energy. Thus, great efforts have been devoted to design new photocatalysts with appropriate band edge positions to effectively utilize visible light, which accounts for about 43% of the incoming solar energy [18,19]. Ever since Zou et al. [20] prepared the new types of oxide semiconductor photocatalyst which could achieve the direct splitting of water under visible light irradiation, visible light driven photocatalyst has become a research focus in photocatalysis field

[21–33].

Among the new visible light driven photocatalysts under investigation, monoclinic scheelite bismuth vanadate (BiVO$_4$) has attracted extensive attention recently because of its unique properties, such as excellent visible light response, chemical stability, nontoxicity as well as relatively high photocatalytic activity for water splitting and removal of organic compounds [34–38]. However, the commercialization of BiVO$_4$ has been limited by poor capability to separate electron-hole pairs and relatively weak ability in utilization sunlight. Thus, further study is necessary to enhance its performance for practical application [39–41].

It is generally known that constructing p-n heterojunction photocatalyst is an ideal method to facilitate the separation of photoexcited electron-hole pairs, and hence enhance the performance of photocatalyst. BiVO$_4$ is an n-type semiconductor, in order to improve the photocatalytic activity of BiVO$_4$, a number of BiVO$_4$-based p-n

heterojunction photocatalysts, such as n-BiVO$_4$/p-Silicon, p-CuO/n-BiVO$_4$, p-BiOI/n-BiVO$_4$, etc., have been synthesized in the past decades [42–46]. For example, Wang et al. have successfully constructed an efficient p–n junction Cu$_2$O/BiVO$_4$ heterogeneous nanostructure for enhancement of visible light photocatalytic properties of BiVO$_4$ nanocrystals [47]. Sun et al. have developed a novel p-Bi$_2$O$_3$/n-BiVO$_4$ nanocomposite with p-n heterojuction structure. Steady state and transient-state photoluminescence spectra prove that the photo-induced charge carriers in the nanocomposite display higher separation and much longer lifetime than those in individual BiVO$_4$ samples, which is attributed to the formation of efficient interfacial electric field between p-Bi$_2$O$_3$ and n-BiVO$_4$ [48]. Wang et al. have reported that n-BiVO$_4$/p-Co$_3$O$_4$ with the high photocatalytic activity can be attributed to the electrocatalytic properties of the Co$_3$O$_4$ cocatalyst and to the formation of a p-n heterojunction at the BiVO$_4$–Co$_3$O$_4$ interface [49]. In our previous study, we have prepared p-n heterojunction photocatalyst n-BiVO$_4$@p-MoS$_2$ with core-shell structure through a facile in-situ hydrothermal method, and the photocatalytic performances of samples were systematically investigated via the photocatalytic reduction of Cr^{6+} and oxidation of crystal violet under visible-light irradiation [50]. These results prove that catalytic performance of p-n heterojunction photocatalysts is indeed better than that of single semiconductor.

Furthermore, the performance of the heterojunction photocatalyst can be greatly improved if the surface of the photocatalyst is modified with noble metal nanoparticles (such as Au and Ag) to form palsmonic heterojunction photocatalyst. Moreover, the obtained noble metal/heterojunction photocatalyst structure can exhibit strong absorbance in the visible light region due to the localized surface plasmon resonance (LSPR) from the collective oscillation of the surface electrons [51,52]. A large number of studies have proved that LSPR can enhance the light absorption and improve charge separation, which in turn enhances the photocatalytic performance [53,54]. Yamashita research group and Huang research group have got a lot outstanding accomplishments to the plasmonic photocatlysis [55–57]. Yang has prepared the Ag/TiO$_2$-N plasmonic photocatalyst with the excellent visible light photocatalytic inactivation of *Acinetobacter baumannii* owing to the enhanced visible light harvesting and the high separation efficiency of photo-induced charge carriers [58]. Our previous studies have shown that the activity of the heterojunction photocatalyst can be further enhanced by depositing Ag nanoparticles on the surface of the heterojunction photocatalyst. Our heterojunction photocatalyst AgVO$_3$/C$_3$N$_4$ fabricated has a reaction rate constant of 0.0552 min^{-1} for the photo-degradation of basic fuchsin (BF) [59]. Further, the plasmonic heterojunction photocatalyst Ag/AgVO$_3$/C$_3$N$_4$, synthesized via a facile one-step in-situ hydrothermal method, reveals an excellent photocatalytic activity for the degradation of BF with an apparent rate constant of 0.0701 min^{-1} which is about 1.3 times higher than that of AgVO$_3$/C$_3$N$_4$ [60]. In addition, we also have synthesized novel Ag/AgVO$_3$/RGO ternary plasmonic photocatalyst through a facile in-situ hydrothermal method, exhibiting excellent light-trapping ability and photocatalytic performance [61].

The above investigations inspired us that one of the best ways to fabricate a highly efficient photocatalyst may be to combine these approaches together, that is, BiVO$_4$-based p-n heterojunction photocatalysts incorporated with silver nanoparticles for LSPR generation. In this study, to test this hypothesis, first, 3D BiVO$_4$ microspheres assembled by 2D BiVO$_4$ nanosheets were prepared via hydrothermal approach. Then, BiVO$_4$-based p-n heterojunction photocatalyst, p-Ag$_2$S/n-BiVO$_4$, was synthesized by depositing p-type Ag$_2$S nanoparticles on the 3D n-type BiVO$_4$ surface. Finally, the plasmonic p-n heterojunction photocatalyst Ag/p-Ag$_2$S/n-BiVO$_4$ was obtained by photoreduction of Ag$^+$ on p-type Ag$_2$S surfaces by photogenerated electron. This facile deposition-photoreduction synthetic route to prepare the plasmonic p-n heterojunction photocatalyst Ag/p-Ag$_2$S/n-BiVO$_4$ is schematically depicted in Fig. 1. Such a 3D hierarchical structure obtained consists of a flower-like BiVO$_4$ sphere and Ag/Ag$_2$S nanoparticles on the surface of

BiVO$_4$. Moreover, the in-situ growth of Ag on Ag$_2$S via photoreduction is an important approach to achieve the robust bonding between Ag and Ag$_2$S, which is essential for the effective charge transfer and separation during photocatalysis. To the best of our knowledge, this novel 3D plasmonic p-n heterojunction photocatalyst Ag/p-Ag$_2$S/n-BiVO$_4$ has not been reported.

Benefiting from the unique structural features, the photocatalytic performance of the novel as-obtained 3D plasmonic p-n heterojunction photocatalyst Ag/p-Ag$_2$S/n-BiVO$_4$ was investigated via the photocatalytic reduction of Cr^{6+} and oxidation of oxytetracycline hydrochloride (OTH) under visible light irradiation. The photocatalytic enhancement mechanism of the plasmonic p-n heterojunction photocatalyst Ag/p-Ag$_2$S/n-BiVO$_4$ was discussed in detail. The facile deposition-photoreduction synthetic strategy to form plasmonic p-n heterojunction photocatalyst may open a new opportunity to develop highly efficient visible-light-driven photocatalyst for environmental applications.

2. Experimental section

2.1. Materials

Bismuth nitrate pentahydrate (Bi(NO$_3$)$_3$·5H$_2$O), sodium orthovanadate dodecahydrate (Na$_3$VO$_4$·12H$_2$O), silver nitrate (AgNO$_3$), and other chemicals used were of analytically pure grade (99%). The above chemical reagents were purchased from Sinopharm Chemical Reagent Co., Ltd. without further purification. Solutions were prepared with ultrapure water.

2.2. Preparation of flower-like BiVO$_4$ microsphere

The flower-like BiVO$_4$ microsphere was synthesized via a facile hydrothermal method. 60 mg Bi(NO$_3$)$_3$·5H$_2$O was dispersed in 40 mL of ultrapure water and subjected to ultrasonication for 5 min. Then, 100 mg Na$_3$VO$_4$·12H$_2$O was added to the solution under vigorous stirring to form an opaque yellow suspension. The mixture was transferred into a Telfon-lined stainless steel autoclave and heated at 160 °C for 8 h. The obtained product was allowed to cool down to the room temperature and washed with ultrapure water and ethanol.

2.3. Preparation of p-Ag$_2$S/n-BiVO$_4$ p-n heterojunction photocatalyst

The p-Ag$_2$S/n-BiVO$_4$ p-n heterojunction photocatalyst was prepared by a simple in-situ deposition method where the Ag$_2$S was formed via an ion-exchange process between Na$_2$S and AgNO$_3$. In a typical process, one mmol as-prepared BiVO$_4$ was dispersed in 50 mL high purity water and the solution was sonicated for 5 min. Then, 0.3 mmol AgNO$_3$ was added to the above homogeneously dispersed solution under violent stirring which was kept for 30 min to dissolve AgNO$_3$ completely. Subsequently, 0.15 mmol Na$_2$S previously dissolved in 50 ml high purity water was added dropwise to the above solution. The solution was kept stirring violently for 7 h in a dark condition. Lastly, the obtained products were centrifuged and washed with high purity water and ethyl alcohol. In addition, the obtained products were dried in 70 °C for 8 h.

2.4. Preparation of Ag/p-Ag$_2$S/n-BiVO$_4$ plasmonic p-n heterojunction photocatalyst

0.5 g p-Ag$_2$S/n-BiVO$_4$ added to 50 mL ethanol was sonicated for 5 min. The suspension was irradiated by ultraviolet light for 5 h. Lastly, Ag/p-Ag$_2$S/n-BiVO$_4$ plasmonic p-n heterojunction photocatalyst was obtained after centrifugation. Briefly, the sample was denoted as 5-Ag/p-Ag$_2$S/n-BiVO$_4$. The number of 5 represents the irradiation time. Similarly, 3-Ag/p-Ag$_2$S/n-BiVO$_4$ and 8-Ag/p-Ag$_2$S/n-BiVO$_4$ were also synthesized by the above procedure except that 3 h and 8 h of
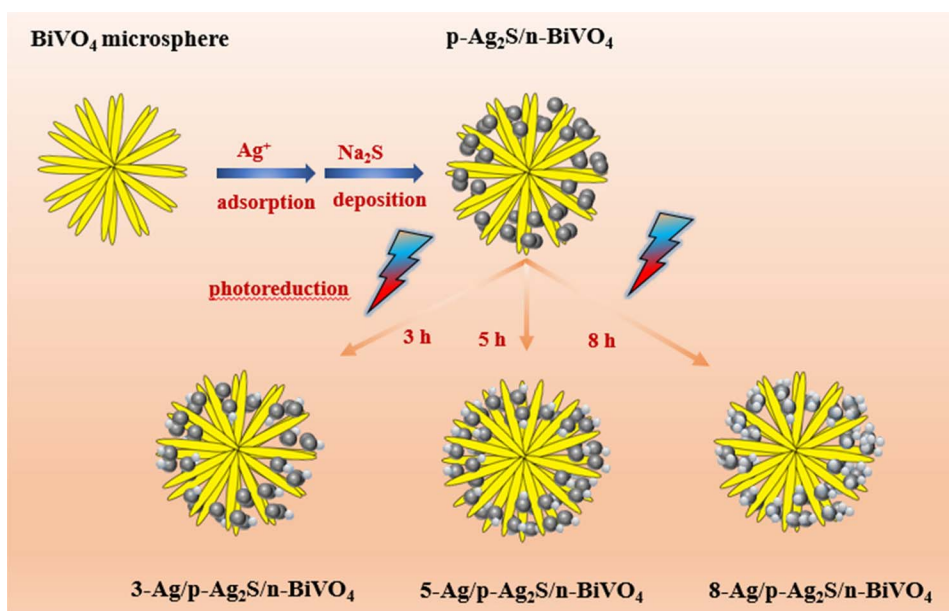
Fig. 1. Schematic illustration of the synthesis of 3D plasmonic p-n heterojunction photocatalyst Ag/p-Ag$_2$S/n-BiVO$_4$.

irradiation times were used, respectively.

2.5. Photocatalytic activities test

The photocatalytic activities of the as-synthesized samples were systematically investigated by the photocatalytic oxidation of OTH and photocatalytic reduction of Cr^{6+} under visible light irradiation. Visible light was generated by a 500 W Xe lamp with a 420 nm cut-off filter to remove light with wavelength < 420 nm. The amount of photocatalyst used was 0.4 g/L, the initial concentrations of Cr^{6+} and OTH are 15 mg/L (which was based on Cr in a dilute K$_2$Cr$_2$O$_7$ solution) and 20 mg/L, respectively. Prior to irradiation, the suspensions, including 50 mL OTH (or Cr^{6+}) solution and 0.02 g as-prepared sample were magnetically stirred for 60 min to reach adsorption-desorption equilibrium in the dark. After illumination, the samples (volume of each is 3 mL) were taken from the reaction suspension, centrifuged at 8000 rpm for 10 min and filtered through a 0.22 m Millipore filter to remove the particles. The filtrate was subsequently analyzed by UV–vis spectroscopy. To ensure the reproducibility of the results, duplicate runs were performed for each condition for averaging the results.

2.6. Analytical methods

The concentration of OTH in solution was determined by UV–vis spectroscopy. The concentration of Cr^{6+} in solution was also determined by UV–vis spectroscopy using diphenylcarbazide reagent as a developer. The photocatalytic oxidation efficiency of OTH and the reduction efficiency of Cr^{6+} were calculated from the following expression:

$$\eta = (C_t - C_0)/ C_0 \times 100\%$$

where η is the photocatalytic degradation efficiency; C_t and C_0 are the concentration of OTH (or Cr^{6+}) before and after photocatalytic reaction.

2.7. Material characterization and simulation

The crystal phase of samples were determined by powder X-ray diffraction (XRD) using a XRD-6000 X-ray diffractometer (SHIMADZU). X-ray photoelectron spectroscopy (XPS) was performed to identify the chemical compositions and the chemical states of the catalysts on a

PHI5000 Versa Probe spectrometer (ULVAC-PHI, Japan). Field emission scanning electron microscope (FESEM) and corresponding energy-dispersive X-ray spectroscopy (EDS) were conducted on a QUANTA FEG 250 scanning electron microscope. The transmission electron microscopy (TEM) and high-resolution transmission electron microscopy (HRTEM) images were obtained on a JEM-200CX instrument. Both UV–vis diffuse reflectance spectra (UV–vis/DRS) and photoluminescence spectra (PL) were recorded to measure the optical properties of the samples by UV–vis spectrometry (UV-3600) and Fluorescence Spectrometry (Horiba HJY FM-4P-TCSPC). The photoelectrochemical characterization was carried out on a CHI760E electrochemical workstation with a standard three-electrode system (Shanghai, China). The samples were loaded onto ITO electrode (1 cm × 2 cm squares) and acted as the working electrode. The counter and reference electrodes were Pt plate and Ag/AgCl electrode. The electrolyte was 0.2 M Na$_2$SO$_4$ aqueous solution and a 500 W Xe lamp was used to provide the light source.

Finite difference time domain (FDTD) simulations were carried out to the model near field distribution of Ag/Ag$_2$S. In the simulations, for simplicity, we assumed that the Ag nanoparticles were uniformly distributed on the x–y plane of the cross section of Ag$_2$S nanoparticle and were embedded in a background medium of water. Illumination of the Ag/Ag$_2$S was simulated with a linearly polarized plane wave, propagating in the +Y direction.

3. Results and discussion

3.1. Structure and morphology of the Ag/p-Ag$_2$S/n-BiVO$_4$ plasmonic p-n heterojunction photocatalyst

The crystallographic structures and phase purities of the as-prepared BiVO$_4$, Ag$_2$S, p-Ag$_2$S/n-BiVO$_4$ and Ag/p-Ag$_2$S/n-BiVO$_4$ photocatalysts were determined using XRD measurements (Fig. 2). All the diffraction peaks are in accordance with the body-centered monoclinic phase of BiVO$_4$ [JCPDS: 14-0666]. No diffraction peak for the Ag$_2$S component can be observed in p-Ag$_2$S/n-BiVO$_4$ sample suggesting that Ag$_2$S is highly dispersed on the BiVO$_4$ surface, and the content is too small to detect using this equipment. In addition, the superposition of the Ag$_2$S and BiVO$_4$ peaks exists at around 32°, the strong diffraction peaks of BiVO$_4$ should have masked the Ag$_2$S diffraction peaks. As for Ag/p-Ag$_2$S/n-BiVO$_4$, the diffraction peaks of Ag cannot be found in the
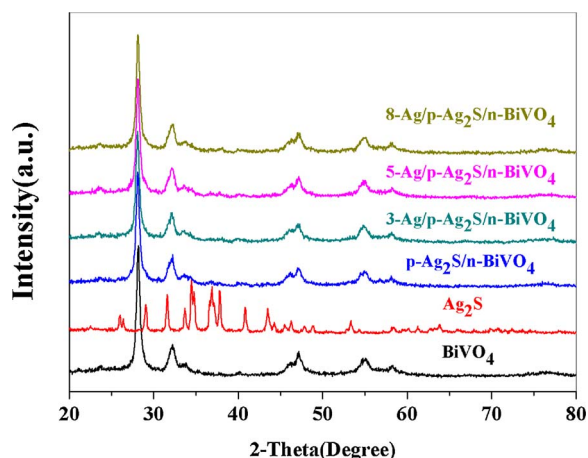
Fig. 2. XRD patterns of the as-prepared samples.

XRD patterns due to its low content or poor crystallinity. In order to further verify the existence of Ag_2S and Ag, the samples were furthered examined by FESEM, TEM and XPS analysis. Meanwhile, the introduction of Ag and Ag_2S has negligible change on the diffraction peak positions and has not lead to the new phase of $BiVO_4$, which suggests that Ag and Ag_2S may be deposited on the surface of the sample instead of covalently incorporating into the crystal lattice of $BiVO_4$.

In order to verify the existence of Ag_2S and the chemical states of Ag species, the X-ray photoelectron spectrum (XPS) of the 5-Ag/p-Ag_2S/n-$BiVO_4$ was measured. Fig. 3a displays the survey of the sample. Chemical binding energies are observed at approximately 284.8, 369.1, 160.7, 529.8, 517.1 and 159.4 eV for C 1s, Ag 3d, S 2p, O 1s, V 2p and Bi 4f, respectively, which shows that the sample surface contains the element of C, Ag, S, O, V and Bi. Information regarding the silver species can be obtained by the high-resolution XPS spectra [62]. From the XPS spectra of Ag 3d (Fig. 3b), it exhibits two individual peaks centered at 367.6 and 373.6 eV, which correspond to Ag $3d_{5/2}$ and Ag $3d_{3/2}$ binding energies, respectively. These two peaks can be further deconvoluted into four bands, i.e. 367.5 and 373.5 eV for Ag^+ $3d_{5/2}$ and $3d_{3/2}$ respectively, and 368.6 and 374.5 eV for $Ag°$ $3d_{5/2}$ and $3d_{3/2}$

[63] respectively, verifying the presence of different valences of silver species. In Fig. 3c, the peak at 160.8 eV correspond to S2p binding energy for Ag_2S, which is consistent with the reported data of Ag_2S [64]. From Fig. 3d, the dominant peak of O 1s locates at 529.8 eV, which suggests the lattice oxygen O^{2-} (in the stronger Bi-O band) [65]. The other two peaks at 532.8 and 531.5 eV are assigned to the O in H_2O and oxygen in the sample surface hydroxyl species, respectively [66,67]. In that case, much oxygen atoms exist on the photocatalyst surface that they can capture the photogenerated electron-hole pairs, further inhibiting the photogenerated electron-hole recombination, increasing the quantum efficiency and prolonging the lifetime of the photoexcited carriers. As a result, the photocatalytic activity of the samples are effectively enhanced. Furthermore, the peaks located at 158.9, 164.2, and 516.8, 524.3 eV are closely consistent with Bi^{3+} and V^{5+} in Fig. 3e and f.

The morphologies of the as-prepared $BiVO_4$, p-Ag_2S/n-$BiVO_4$ and 5-Ag/p-Ag_2S/n-$BiVO_4$ were investigated by FESEM. In Fig. 4a and b, the $BiVO_4$ powder shows a uniform flower-like 3D microsphere shape with a size of 2–4 μm. Through careful observation, we find that this flower-like 3D microsphere is assembled by 2D $BiVO_4$ nanosheets. Compared to the pure $BiVO_4$, the surfaces of p-Ag_2S/n-$BiVO_4$ (Fig. 4c and d) and 5-Ag/p-Ag_2S/n-$BiVO_4$ (Fig. 4e and f) become rough which indicates that some Ag and or Ag_2S nanoparticles are gathered on the petals. No obvious change in the morphology of the samples are noticed after deposition of Ag and or Ag_2S, which is in agreement with the XRD results.

In order to obtain the detailed morphology and microstructure, the pure $BiVO_4$ and 5-Ag/p-Ag_2S/n-$BiVO_4$ were examined by TEM and HRTEM. Fig. 4g shows that the 2D $BiVO_4$ nanosheets are clustered to form 3D flower-like $BiVO_4$ microspheres with a diameter of around 2 um. Comparing the TEM images of $BiVO_4$ (Fig. 4g) with that of 5-Ag/p-Ag_2S/n-$BiVO_4$ (Fig. 4h and i) further indicates that the Ag and or Ag_2S nanoparticles are successfully deposited on the $BiVO_4$ microsphere surfaces. To elaborate the cystallographic structure of the sample, HRTEM measurements are also performed. From the HRTEM image in Fig. 4j, the interplanar distances are calculated to be 0.27 nm and 0.23 nm corresponding to the (1 2 2) crystal plane of Ag_2S and (1 1 1) crystal plane of Ag, respectively [68]. The clear interface between the two phases would contribute to the separation of the photo-generated charge carriers.
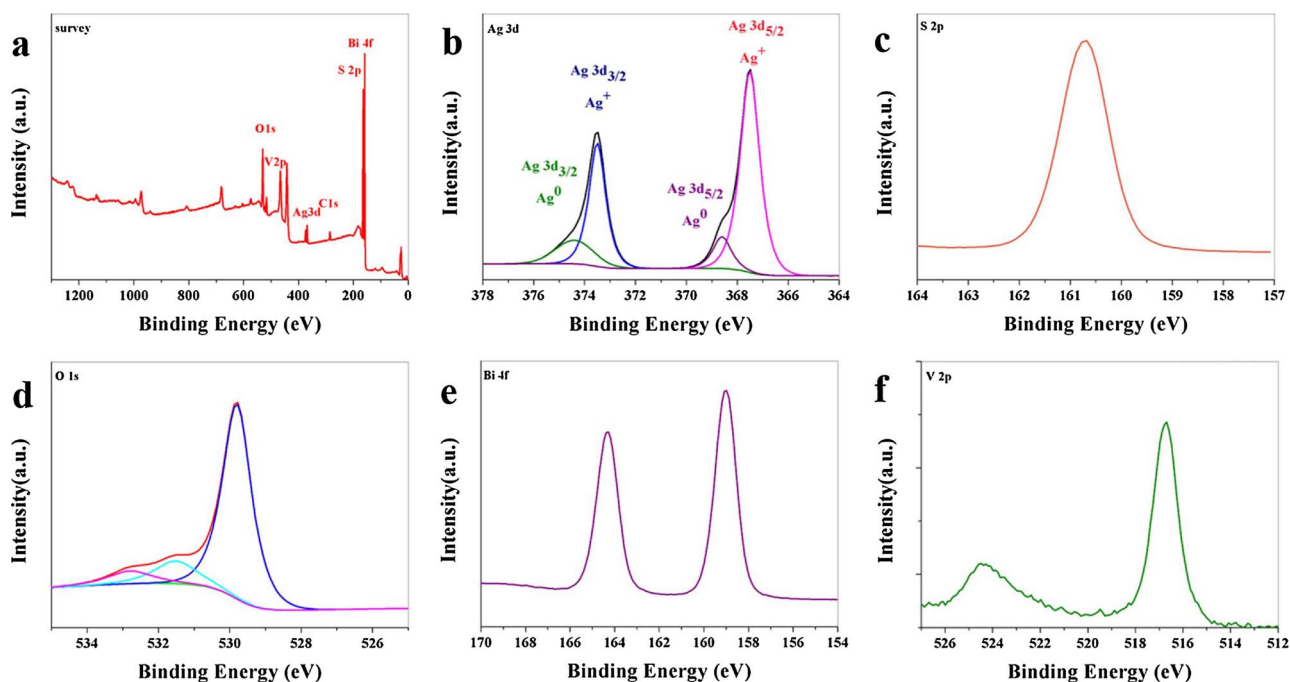

Fig. 3. (a) XPS spectra of survey; (b) XPS spectra of Ag 3d; (c) XPS spectra of S 2p; (d) XPS spectra of O 1s; (e) XPS spectra of Bi 4f; (f) XPS spectra of V 2p.
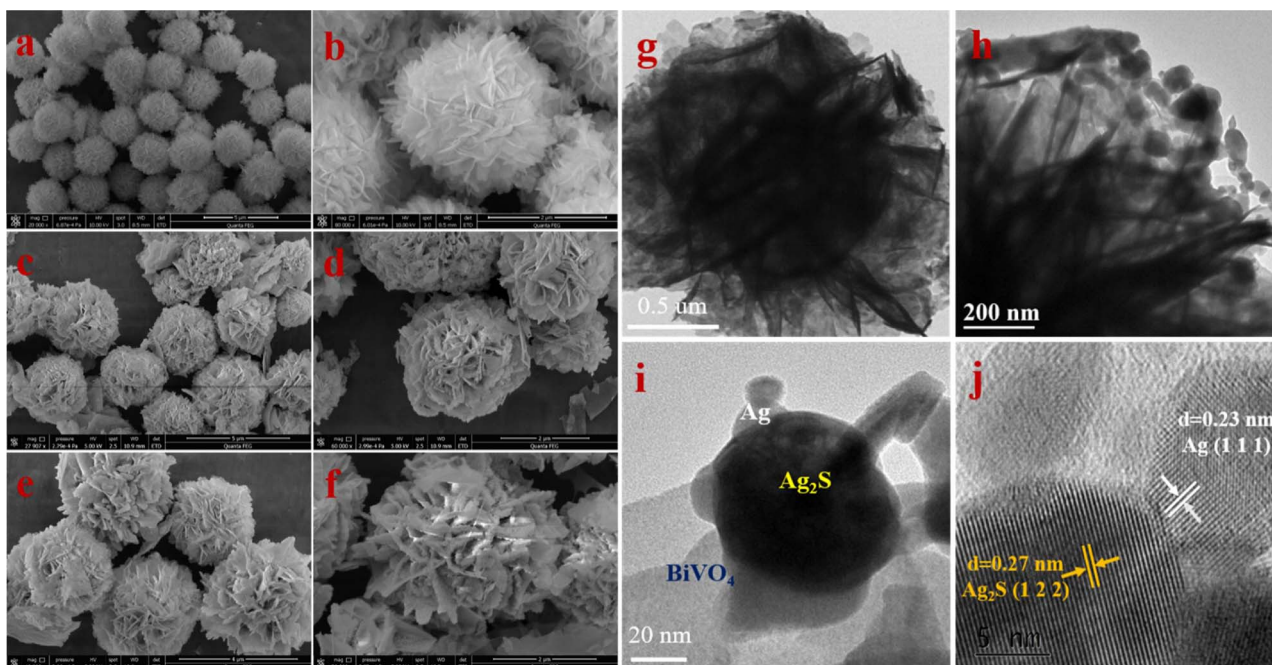
Fig. 4. (a–b) The FESEM image of $BiVO_4$, (c–d) The FESEM image of $p-Ag_2S/n-BiVO_4$, (e–f) The FESEM image of $5-Ag/p-Ag_2S/n-BiVO_4$, (g) TEM image of $BiVO_4$, (h–i) TEM image of $5-Ag/p-Ag_2S/n-BiVO_4$, and (j) HRTEM image of $5-Ag/p-Ag_2S/n-BiVO_4$.
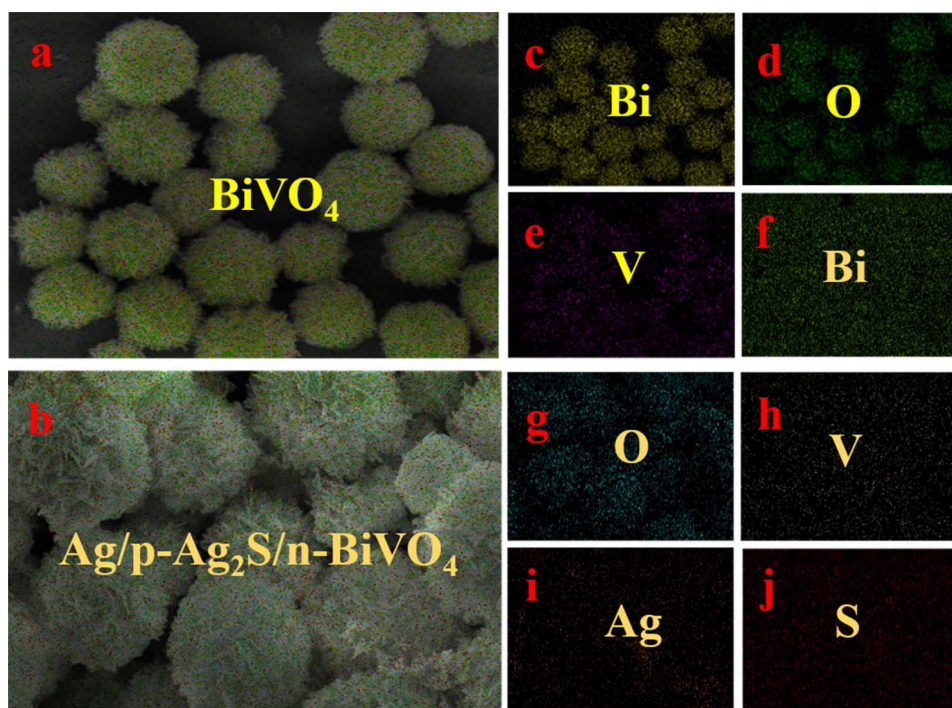

Fig. 5. SEM-EDS elemental mapping of (a) $BiVO_4$, (b) $Ag/p-Ag_2S/n-BiVO_4$, (c–e) Bi, O, V element of $BiVO_4$, and (f–j) Bi, O, V, Ag, S element of $Ag/p-Ag_2S/n-BiVO_4$.

Fig. 5a and b shows the SEM-EDS elemental mapping of $BiVO_4$ and $Ag/p-Ag_2S/n-BiVO_4$, respectively. The 2D-projected elemental mapping of $BiVO_4$ sample discloses in Fig. 5a, the pure $BiVO_4$ only possesses the elements of Bi, O and V (Fig. 5c–e). Besides, the SEM-EDS elemental mapping in Fig. 5b verifies that the $Ag/p-Ag_2S/n-BiVO_4$ is composed of Bi, O, V, Ag and S (Fig. 5f–j).

Based on the above XPS, SEM, TEM, HRTEM, BET and SEM-EDS results, it can be inferred that $Ag/p-Ag_2S/n-BiVO_4$ photocatalysts have been successfully fabricated.

3.2. Optical properties of the $Ag/p-Ag_2S/n-BiVO_4$ plasmonic p-n heterojunction photocatalyst

The optical properties of the as-prepared $BiVO_4$, $p-Ag_2S/n-BiVO_4$, and $Ag/p-Ag_2S/n-BiVO_4$ photocatalysts were exploited with the UV–vis absorption spectra and the photoluminescence spectra. UV–vis absorption spectra of $BiVO_4$, $p-Ag_2S/n-BiVO_4$, and $Ag/p-Ag_2S/n-BiVO_4$ are illustrated in Fig. 6a. For the pure $BiVO_4$, a strong absorption at wavelength shorter than around 500 nm attribute to the intrinsic band gap absorption. Interestingly, compared with $BiVO_4$ and $p-Ag_2S/n-$
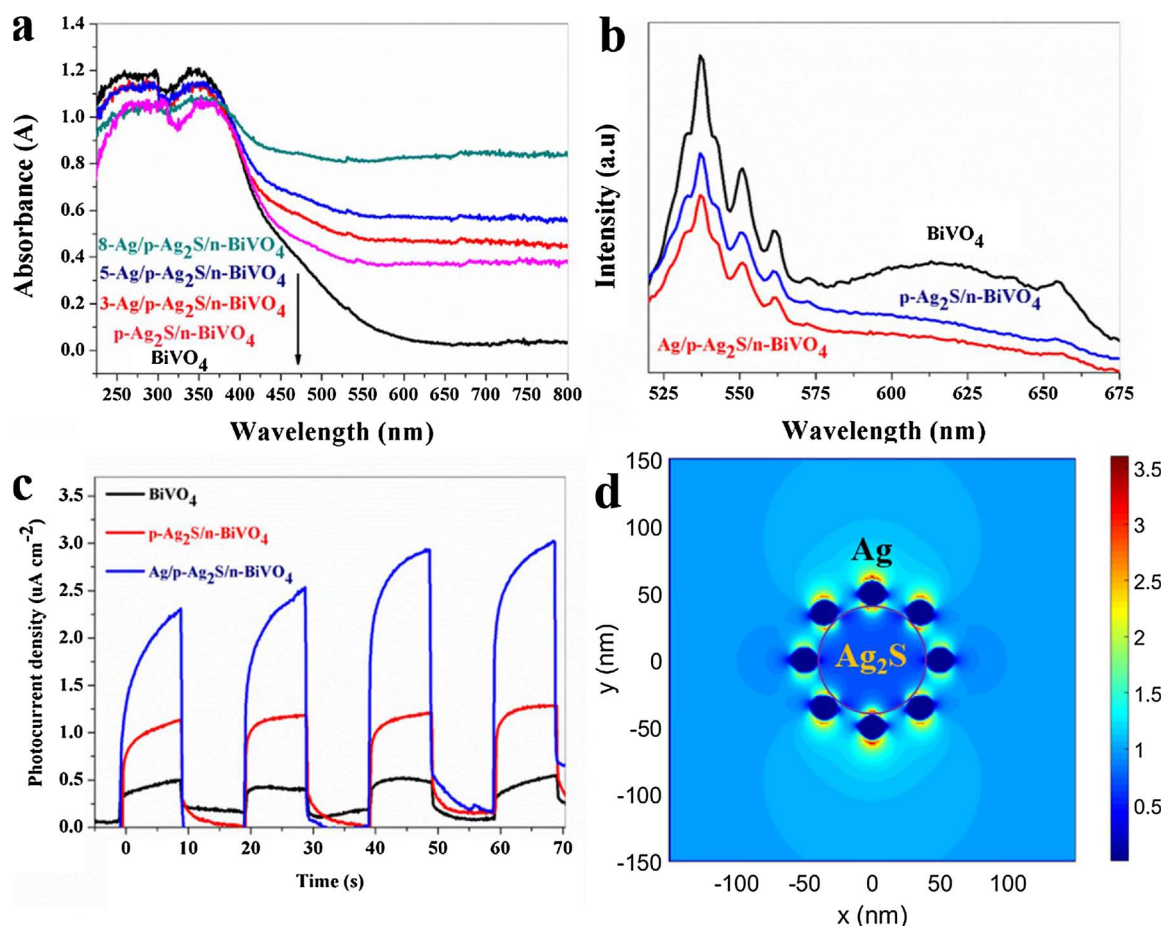
Fig. 6. (a) UV–vis absorption spectra of as-prepared samples, (b) PL spectra of as-prepared samples, (c) photocurrent of samples, (d) Electric field distributions calculated at the cross-sections of Ag/Ag$_2$S using the FDTD method.

$BiVO_4$, the optical absorption of Ag/p-Ag$_2$S/n-BiVO$_4$ samples in the visible regions all raise, which means that the samples would display better photocatalytic performance under the visible light irradiation. The phenomenon is ascribed to the existence of Ag nanoparticles in the sample surface. On the one hand, Ag nanopaticles have darken color to enhance the visible light absorbance. On the other hand, it could arouse a strong LSPR absorption.

Since the recombination of the photogenerated electron-hole pairs is recognized as the critical factor influencing the photocatalytic activity of the catalysts, the charge efficiency were obtained by PL spectrum. The lower fluorescence emission intensity implies the higher separation rate of electron-hole pairs. The PL spectra of all the samples were excited with the wavelength of 425nm (Fig. 6b). For the pure BiVO$_4$, it has a wide emission peak centered at around 550 nm, which is considered to result from the recombination of the hole formed in the O 2p band and the electron in the V 3d band [69]. Moreover, the relative intensity of the emission spectra of BiVO$_4$ is the highest, indicating that holes and electrons are easy to recombine. The relative intensity of p-Ag$_2$S/n-BiVO$_4$ is lower than that of BiVO$_4$, which may be attributed to the efficient charge transfer between Ag$_2$S and BiVO$_4$. As expected, once Ag depositing on the p-Ag$_2$S/n-BiVO$_4$ surface further, the relative intensity of its fluorescence emission is even lower than the p-Ag$_2$S/n-BiVO$_4$, displaying that by the incorporation of Ag nanoparticles and p-n heterojunction (p-Ag$_2$S/n-BiVO$_4$) can further enhance the carrier separation.

Photocurrent measurements were also taken to investigate the photoresponses of BiVO$_4$, p-Ag$_2$S/n-BiVO$_4$ and Ag/p-Ag$_2$S/n-BiVO$_4$. The photocurrent value indirectly reflects the separation efficiency of the photogenerated charge carriers. As shown in Fig. 6c, it is clear that

Ag/p-Ag$_2$S/n-BiVO$_4$ performs the highest photocurrent intensity among these samples. Therefore, Ag/p-Ag$_2$S/n-BiVO$_4$ is more capable of producing charge carriers and separating electron-hole pairs than p-Ag$_2$S/n-BiVO$_4$ and BiVO$_4$.

In order to examine the LSPR and the electric field enhancement caused by the Ag nanoparticles, the electric field distribution was simulated by using the FDTD method. For simplicity, the model showed in Fig. 6d is the cross sectional view between the Ag and Ag$_2$S nanoparticles. The importance of the intense local fields is shown in Fig. 6d, illustrating a cross-sectional plot of the electric field distribution of the hot spot regions in the y-dimension. The local "hot spots" can be seen in regions among nearly touching Ag nanoparticles, the electric field intensity between the Ag$_2$S and the Ag nanoparticles is much higher than that of the incident electromagnetic radiation under 420 nm wavelength illuminations because of the LSPR of the Ag nanoparticles. This process is helpful for the rapid formation of electron–hole pairs near the surface of the sample, which evidently explain the reason why this plasmonic photocatalyst can display excellent visible light catalytic activity.

3.3. Evaluation of photocatalytic activity

The photocatalytic activities of BiVO$_4$, p-Ag$_2$S/n-BiVO$_4$ and Ag/p-Ag$_2$S/n-BiVO$_4$ were investigated by the photocatalytic oxidation of OTH and reduction of Cr^{6+} under visible light irradiation. Prior to the photocatalytic experiment, a dark adsorption was carried out for 60 min to achieve an equilibrium adsorption state. In addition, as the reference experiments, the photolysis of OTH without the photocatalysts was also performed.
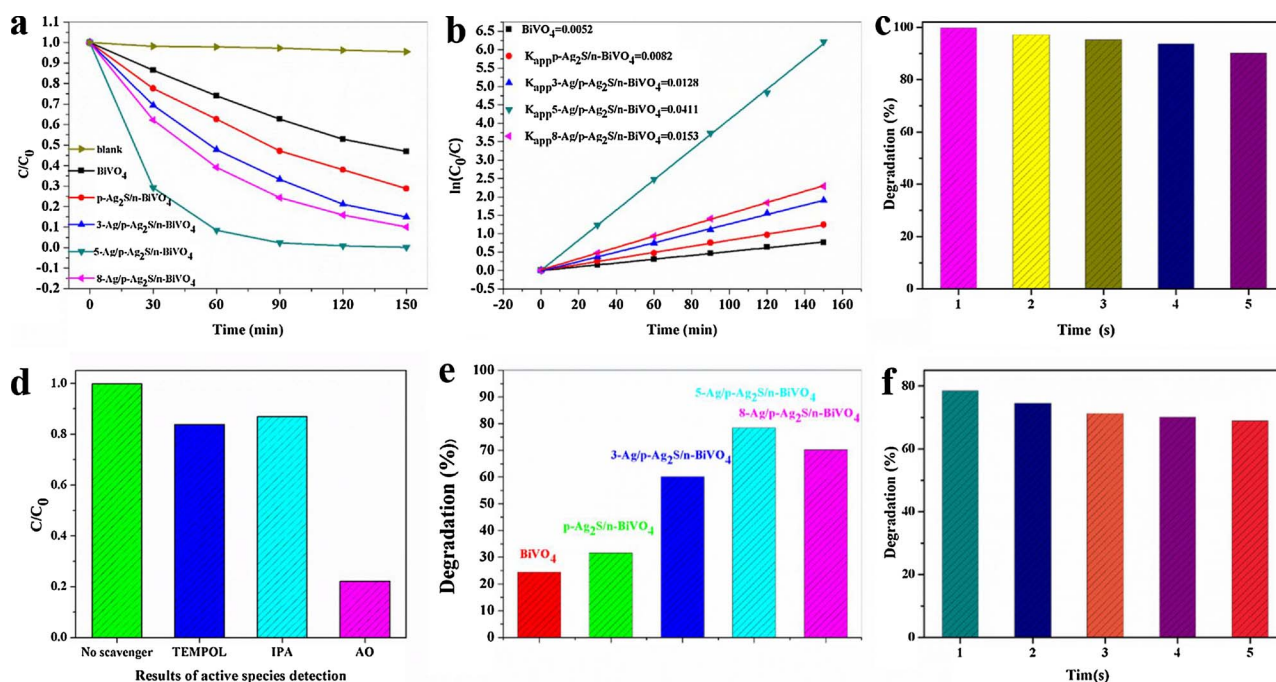
Fig. 7. (a) Photocatalytic activities and (b) pseudo-first-order kinetics of the as-prepared photocatalysts for OTH degradations, (c) five recycling runs of 5-Ag/p-Ag$_2$S/n-BiVO$_4$ for OTH degradations, (d) the effect of different quenchers on the photocatalytic oxidation of OTH, (e) photocatalytic reduction activities of as-prepared photocatalysts for Cr^{6+} reduction, (f) 5 recycling runs of 5-Ag/p-Ag$_2$S/n-BiVO$_4$ for Cr^{6+} reduction.

Fig. 7a illustrates the different photocatalytic oxidation of OTH over samples. Among the as-prepared samples, 5-Ag/p-Ag$_2$S/n-BiVO$_4$ exhibits the highest photocatalytic oxidation activity, and the oxidation degradation of OTH is 99.8% after 150 min of visible light irradiation. It is clear that by adjusting the Ag content on p-Ag$_2$S/n-BiVO$_4$ surfaces, the photocatalysis performance can be further improved. However, the increasing Ag content could cover up the surface, which not only retard the absorption of light but also reduce the surface area available for the reaction on the sample, hence reducing the photocatalytic activity (e.g. 8-Ag/p-Ag$_2$S/n-BiVO$_4$). Following the Langmuir-Hinshelwood model, the apparent reaction rate constants of the degradation could be acquired from the following equation: ln(C$_0$/C$_t$) = k$_{app}$t, where C$_0$ represents the initial concentration of OTH solution, C$_t$ represents the concentration of OTH at time t, and the slope k$_{app}$ represents the apparent reaction rate constant. Fig. 7b clearly showed that the experimental data were in accordance with the pseudo first order kinetics model. As shown in Fig. 7b, 5-Ag/p-Ag$_2$S/n-BiVO$_4$ demonstrates the highest value of k$_{app}$ (0.0411 min^{-1}), which is about 7.9 and 5.0 times higher than that of pure BiVO$_4$ (0.0052 min^{-1}) and p-Ag$_2$S/n-BiVO$_4$ (0.0082 min^{-1}), respectively. In addition, the stability of photocatalysts is an important parameter for their practical applications. Therefore, the stability and the reusability of the 5-Ag/p-Ag$_2$S/n-BiVO$_4$ plasmonic p-n heterojunction photocatalyst during OTH oxidation degradation were investigated (Fig. 7c). The ability of 5-Ag/p-Ag$_2$S/n-BiVO$_4$ for the oxidation degradation of OTH has barely declined after five cycling runs. Obviously, the photocatalyst is stable during the photocatalytic oxidation process.

The photocatalytic reduction activities of BiVO$_4$, p-Ag$_2$S/n-BiVO$_4$ and Ag/p-Ag$_2$S/n-BiVO$_4$ samples were also evaluated by the reduction of Cr^{6+} solution under visible light irradiation, as shown in Fig. 7e. The results are similar to the photocatalytic oxidation of OTH, and the 5-Ag/p-Ag$_2$S/n-BiVO$_4$ sample exhibits the highest photocatalytic reduction activity among these samples. The stability of the 5-Ag/p-Ag$_2$S/n-BiVO$_4$ during the photocatalytic reduction of Cr^{6+} was also investigated, as shown in Fig. 7f, the sample exhibited adequate stability.

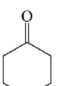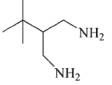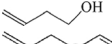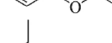### 3.4. The underlying photocatalytic mechanism
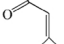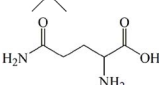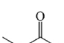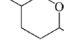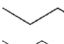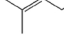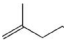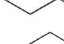
It is well known that photogenerated electrons play a key role in the photocatalytic reduction process, while there are a lot of main reactive oxygen species involved in the photocatalytic oxidation reaction, such as ·O$_2^-$, h$^+$ and ·OH [70–72]. In order to detect the effect of these reactive species on the photocatalytic oxidation of OTH, 4-hydroxy-2,2,6,6-tetramethylpiperidine-N-oxyl (TEMPOL), ammonium oxalate (AO) and isopropanol (IPA) were adopted to quench ·O$_2^-$, h + and ·OH, respectively. The comparative experiment with no quencher was conducted under otherwise identical conditions. As a result of quenching, photocatalytic oxidation would be partly suppressed and the value of photocatalytic oxidation efficiency was lowered. The lower the value of photocatalytic oxidation efficiency is caused by the scavengers, the more important role the corresponding oxidizing species plays in the photocatalytic oxidation. From Fig. 7d, the photocatalytic oxidation degradation of OTH decreased with the addition AO, indicating that h$^+$ participated in the system as the main active species. However, TEMPOL and IPA show little effect on the OTH degradation, which indicates that ·O$_2$- and ·OH are not the main reactive species in the photocatalytic oxidation process.

The intermediates and products formed in the photocatalytic oxidation degradation of OTH were identified by the analysis of mass spectra obtained from GC-MS. Scice h$^+$ is nonselective radicals, more reactive sites are available for the radicals to attack, which makes the reaction products became more complex. Table 1 lists main fragments (m/z) and retention time (min) obtained for 13 intermediate products. The intermediate products are mainly produced by open-ring reactions and cleavage of the central carbon. The intermediates (product 1,7, and 12) are derived through the open-ring reactions, and following by the cleavage of the central carbon to produce smaller organic molecules (product 2– 6, 8–11, and 13).

Based on the above-described experimental results, the mechanism of photocatalytic oxidation and reduction of pollutants over the Ag/p-Ag$_2$S/n-BiVO$_4$ plasmonic p-n heterojunction photocatalyst under visible light irradiation is proposed, as illustrated in Fig. 8.
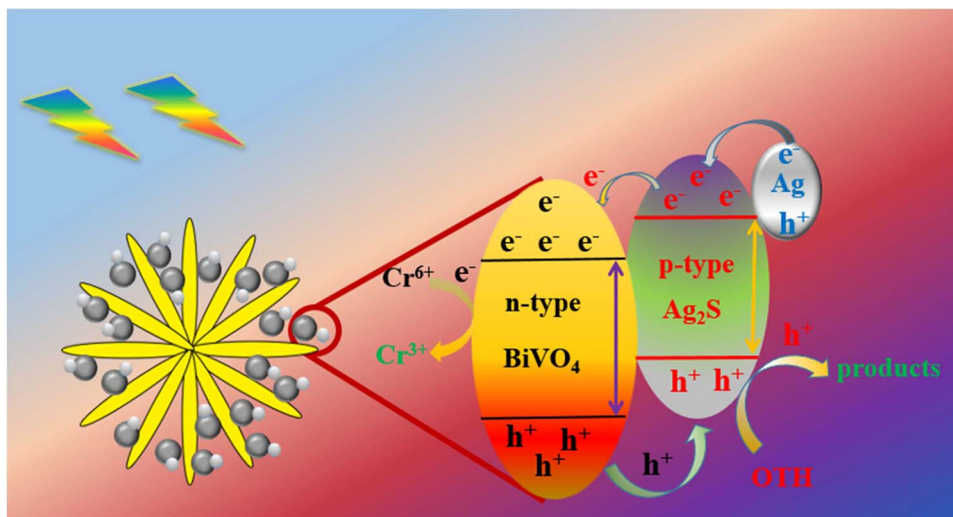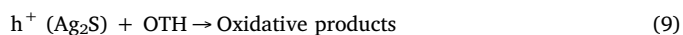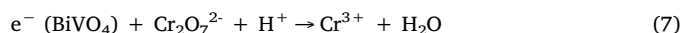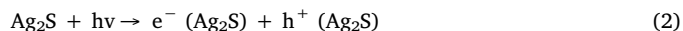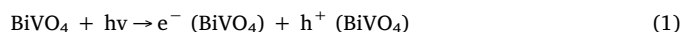
Firstly, the whole photocatalytic process is initiated by the

Table 1
Identification of the intermediates of OTH by GC-MS.

Product	Retention Time/min	m/z	Molecular Structure
1	6.685	98	
2	7.195	130	
3	7.555	86	
4	8.200	84	
5	8.565	98	
6	9.155	146	
7	12.060	128	
8	12.410	85	
9	13.820	152	
10	14.655	156	
11	15.260	102	
12	19.860	150	
13	24.950	156	

Secondly, LSPR generated electrons formed on the surface of Ag nanoparticles transfer to the conduction band of p-type Ag_2S, and then the electrons could migrate from p-type Ag_2S to the conduction of n-type $BiVO_4$ (Eqs. (4)–(6)). Under the circumstances, a large number of electrons are formed on the surface of n-type $BiVO_4$. Meanwhile, the reduction potential of $O_2/\cdot O_2-$ is -0.33 eV [73], the CB edge potential of n-type $BiVO_4$ (0.29 eV) is not negative enough to reduce O_2 to $\cdot O_2-$ radicals. Therefore, the enriched electrons on the surface of $BiVO_4$ could not be trapped by the molecular oxygen in the solution to form $\cdot O_2-$. For the mechanism of photocatalytic reduction of Cr^{6+}, Fu et al. have published a series of important papers proposing that Cr^{6+} captures the photo-excited conduction band electrons and is reduced (Eq. (7)), H_2O gets the valence band holes (Eq. (8)) [74–77]. Moreover, the VB potential of p-type Ag_2S is 0.92 eV. It is not enough positive compared with the standard reduction potential of $\cdot OH/H_2O$ (2.27 eV) or $\cdot OH/OH-$(2.38 eV) [78], indicating that the $h+$ enriched in p-type Ag_2S cannot oxidize H_2O and $OH-$ into $\cdot OH$ radicals, hence not $\cdot OH$ radical but the $h+$ in the valence band of p-type Ag_2S can oxidize OTH to smaller molecules(Eq. (9)). The reactive species experiment has also confirmed that $h+$ radicals are the main reactive species in the photocatalytic oxidation of OTH. In order to further verify that h^+, not $\cdot OH$ ridicals, is the main active species in the photocatalytic oxidation of OTH, the EPR technique with DMPO was used to detect the $\cdot OH$ radicals. The DMPO-$\cdot OH$ signal is not observed in the presence of Ag/p-Ag_2S/n-$BiVO_4$in DMSO solution. But for the Ag_3PO_4, which can oxidize H_2O and $OH-$ into $\cdot OH$ radicals, produces the DMPO-$\cdot OH$ signal (Fig. 9). These results strongly suggest that h^+, not $\cdot OH$ ridicals, is the main active species during the photocatalytic oxidation of OTH process.

$$BiVO_4 + hv \rightarrow e^- (BiVO_4) + h^+ (BiVO_4) \tag{1}$$

$$Ag_2S + hv \rightarrow e^- (Ag_2S) + h^+ (Ag_2S) \tag{2}$$

$$Ag + hv \rightarrow Ag^* \tag{3}$$

$$Ag^* \rightarrow e^- (Ag_2S) \tag{4}$$

$$e^- (Ag_2S) \rightarrow e^- (BiVO_4) \tag{5}$$

$$h^+ (BiVO_4) \rightarrow h^+ (Ag_2S) \tag{6}$$

$$e^- (BiVO_4) + Cr_2O_7{}^{2-} + H^+ \rightarrow Cr^{3+} + H_2O \tag{7}$$

$$H_2O + h^+ (Ag_2S) \rightarrow H^+ + O_2 \tag{8}$$

$$h^+ (Ag_2S) + OTH \rightarrow Oxidative\ products \tag{9}$$

absorption of photons with energy equal or higher than the band gap, which leads to the electron-hole pairs generated from the photoexcited semiconductor components (p-type Ag_2S and n-type $BiVO_4$) and the plasmonexcited Ag nanoparticles (Eqs. (1)–(3)). Both the conduction band and valence band positions of p-type Ag_2S are higher than those of n-type $BiVO_4$, so the photogenerated electrons from the CB of p-type Ag_2S are transferred to the CB of n-type $BiVO_4$, while the photogenerated holes from the VB of n-type $BiVO_4$ are transferred to the VB of p-type Ag_2S, which makes charge separation more efficient.

Fig. 8. The photocatalysis enhancement mechanism of plasmonic p-n heterojunction photocatalyst.
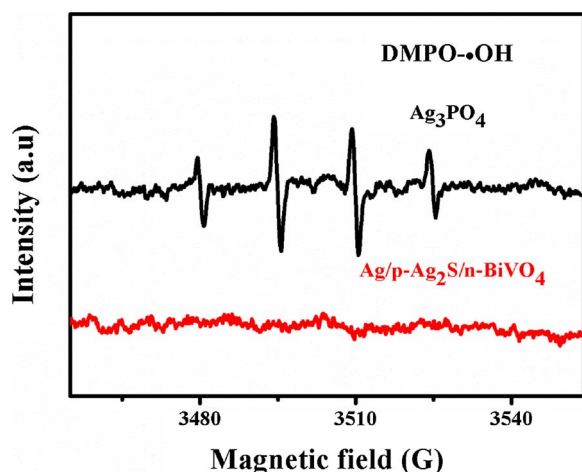
Fig. 9. Spin-trapping EPR spectra of the samples.

4. Conclusions

A novel 3D Ag/p-Ag$_2$S/n-BiVO$_4$plasmonic p-n heterojunction photocatalyst was successfully fabricated via a deposition-photoreduction reaction. The structures, morphologies, and optical properties of the obtained photocatalysts were comprehensively characterized by XRD, XPS, SEM, TEM, HRTEM, SEM-EDS elemental mapping, UV–vis and PL. The photocatalytic performances of the as-prepared samples were systematically investigated via the photocatalytic oxidation of OTH and reduction of Cr^{6+} under visible-light irradiation. The 5-Ag/p-Ag$_2$S/n-BiVO$_4$ plasmonic p-n heterojunction photocatalyst exhibits excellent photocatalytic performance, which can be attributed to the enhanced absorbance in the visible light region, the facilitated charge transfer, and the suppressed recombination of electron-hole pairs in the Ag/p-Ag$_2$S/n-BiVO$_4$. The results of active species detection reveal that h + radical is the main reactive species in the photocatalytic oxidation of OTH. Moreover, 13 photocatalytic degradation intermediates and products of OTH were also identified by the gas chromatography-mass spectrometer (GC–MS). Finally, the photocatalytic enhancement mechanism over Ag/p-Ag$_2$S/n-BiVO$_4$plasmonic p-n heterojunction photocatalyst was discussed in detail.

References

[1] F. Liang, Y.F. Zhu, Appl. Catal. B 180 (2016) 324–329.
[2] K. Mori, K. Miyawaki, H. Yamashita, ACS Catal. 6 (2016) 3128–3135.
[3] X. Li, J. Zhu, H.X. Li, Appl. Catal. B 123 (2012) 174–181.
[4] H.B. Yin, Y. Kuwahara, K. Mori, H.F. Cheng, M.C. Wen, Y.N. Huo, H. Yamashita, J. Phys. Chem. C 121 (2017) 23531–23540.
[5] M. Zhang, W.J. Jiang, D. Liu, J. Wang, Y.F. Liu, Y.Y. Zhu, Y.F. Zhu, Appl. Catal. B 183 (2016) 263–268.
[6] P. Verma, Y. Kuwahara, K. Mori, H. Yamashita, Appl. Catal. B 23 (2017) 3616–3622.
[7] Y.Y. Zhu, Y.J. Wang, Q. Ling, Y.F. Zhu, Appl. Catal. B 200 (2017) 222–229.
[8] M.C. Wen, K. Mori, Y. Kuwahara, H. Yamashita, ACS Energy Lett. 2 (2016) 1–7.
[9] Z.J. Li, X.B. Li, J.J. Wang, S. Yu, C.B. Li, C.H. Tung, L.Z. Wu, Energy Environ. Sci. 6 (2013) 465–469.
[10] D.Q. Zhang, M.C. Wen, S.S. Zhang, P.J. Liu, W. Zhu, G.S. Li, H.X. Li, Appl. Catal. B 147 (2014) 610–616.
[11] S. Jo, P. Verma, Y. Kuwahara, K. Mori, W.Choi H. Yamashita, J. Mater. Chem. A 5 (2017) 21883–21892.
[12] B. Cao, G.S. Li, H.X. Li, Appl. Catal. B 194 (2016) 42–49.
[13] M.K. Mishra, S. Chattopadhyay, A. Mitra, G. De, Ind. Eng. Chem. Res. 54 (2015) 928–937.
[14] Y.N. Huo, X.F. Chen, J. Zhang, G.F. Pan, J.P. Jia, H.X. Li, Appl. Catal. B 148 (2014) 550–556.
[15] J.G. Wang, P. Zhang, X. Li, J. Zhu, H.X. Li, Appl. Catal. B 134 (2013) 198–204.
[16] B. Liu, L.M. Liu, X.F. Lang, H.Y. Wang, X.W. (David) Lou, E.S. Aydil, Energy Environ. Sci. 7 (2014) 2592–2597.
[17] T. Kamegawa, S. Matsuura, H. Seto, H. Yamashita, Angew. Chem. Int. Ed. 52 (2013) 916–919.
[18] X.R. Li, J.G. Wang, Y. Men, Z.F. Bian, Appl. Catal. B 187 (2016) 115–121.
[19] C. Tang, L.F. Liu, Y.L. Li, Z.F. Bian, Appl. Catal. B 201 (2017) 41–47.
[20] J.J. Sun, X.Y. Li, Q.D. Zhao, M.O. Tadé, S.M. Liu, J. Mater. Chem. A 3 (2015) 21655–21663.
[21] X.F. Zhang, B.Y. Zhang, K. Cao, J. Brillet, J.Y. Chen, M.K. Wang, Y. Shen, J. Mater. Chem. A 3 (2015) 21630–21636.
[22] Z.G. Zou, J.H. Ye, K. Sayama, H. Arakawa, Nature 414 (2001) 625–627.
[23] Y.Y. Zhu, Q. Ling, Y.F. Liu, H. Wang, Y.F. Zhu, Appl. Catal. B 187 (2016) 204–211.
[24] G.X. Zhu, J.G. Zhu, W.J. Jiang, Z.J. Zhang, J. Wang, Y.F. Zhu, Q.F. Zhang, Appl. Catal. B 209 (2017) 729–737.
[25] L.G. Xia, J. Bai, J.H. Li, Q.Y. Zeng, L.S. Li, B.X. Zhou, Appl. Catal. B 204 (2017) 127–133.
[26] Y. Li, W.Q. Cui, Li Liu, R.L. Zong, W.Q. Yao, Y.H. Liang, Y.F. Zhu, Appl. Catal. B 199 (2016) 412–423.
[27] W. Zhu, P.J. Liu, S.N. Xiao, W.C. Wang, D.Q. Zhang, H.X. Li, Appl. Catal. B 172 (2015) 46–51.
[28] J. Li, X. Gao, B. Liu, Q.L. Feng, X.B. Li, M.Y. Huang, Z.F. Liu, J. Zhang, C.H. Tung, L.Z. Wu, J. Am. Chem. Soc. 138 (2016) 3954–3957.
[29] K.F. Zhang, Y.X. Liu, J.G. Deng, S.H. Xie, H.X. Lin, X.T. Zhao, J. Yang, Z. Han, H.X. Dai, Appl. Catal. B 202 (2017) 569–579.
[30] L.Z. Wu, B. Chen, Z.J. Li, C.H. Tung, Acc. Chem. Res. 47 (2014) 2177–2185.
[31] Y. Zhang, W.Q. Cui, W.J. An, L. Liu, Y.H. Liang, Y.F. Zhu, Appl. Catal. B 221 (2018) 36–46.
[32] X.Y. Chen, L.F. Liu, Y.W. Feng, L.F. Wang, Z.F. Bian, H.X. Li, Z.L. Wang, Mater. Today 20 (2017) 501–506.
[33] Y.W. Feng, L.L. Ling, Y.X. Wang, Z.M. Xu, F.L. Cao, H.X. Li, Z.F. Bian, Nano Energy 40 (2017) 481–486.
[34] K.F. Zhang, Y.X. Liu, J.G. Deng, S.H. Xie, X.T. Zhao, J. Yang, Z. Han, H.X. Dai, Appl. Catal. B 224 (2018) 350–359.
[35] M. Ou, S.P. Wan, Q. Zhong, S.L. Zhang, Y. Song, L.N. Guo, W. Cai, Y.L. Xu, Appl. Catal. B 221 (2018) 97–107.
[36] J.M. Wu, Y. Chen, L. Pan, P.H. Wang, Y. Cui, D.C. Kong, L. Wang, X.W. Zhang, J.J. Zou, Appl. Catal. B 221 (2018) 187–195.
[37] N.K. Veldurthi, N.K. Eswar, S.A. Singh, G. Madras, Appl. Catal. B 220 (2018) 512–523.
[38] F.Q. Zhou, J.C. Fan, Q.J. Xu, Y.L. Min, Appl. Catal. B 201 (2017) 77–83.
[39] H.Y. Li, Y.J. Sun, B. Cai, S.Y. Gan, D.X. Han, L. Niu, T.S. Wu, Appl. Catal. B 170 (2015) 206–214.
[40] H. Ullah, A.A. Tahir, T.K. Mallick, Appl. Catal. B 224 (2018) 895–903.
[41] F. Chen, Q. Yang, X.M. Li, G.M. Zeng, D.B. Wang, C.G. Niu, J.W. Zhao, H.X. An, T. Xie, Y.C. Deng, Appl. Catal. B 200 (2017) 330–342.
[42] H.W. Huang, Y. He, X. Du, P.K. Chu, Y.H. Zhang, A.C.S. Sustain. Chem. Eng. 3 (2015) 3262–3273.
[43] K.H. Ye, Z.S. Chai, J.W. Gu, X. Yu, C.X. Zhao, Y.M. Zhang, W.J. Mai, Nano Energy 18 (2015) 222–231.
[44] Y.X. Yang, J.R. Wang, J. Zhao, B.A. Nail, X. Yuan, Y.H. Guo, F.E. Osterloh, ACS Appl. Mater. Interfaces 7 (2015) 5959–5964.
[45] W.Z. Wang, J. Wang, Z.Z. Wang, X.Z. Wei, L. Liu, Q.S. Ren, W.L. Gao, Y.J. Liang, H.L. Shi, Dalton Trans. 43 (2014) 6735–6743.
[46] M. Zhong, T. Hisatomi, Y.B. Kuang, J. Zhao, M. Liu, A. Iwase, Q.X. Jia, H. Nishiyama, T. Minegishi, M. Nakabayashi, N. Shibata, R. Niishiro, C. Katayama, H. Shibano, M. Katayama, A. Kudo, T. Yamada, K. Domen, J. Am. Chem. Soc. 137 (2015) 5053–5060.
[47] W.Z. Wang, X.W. Huang, S. Wu, Y.X. Zhou, L.J. Wang, H.L. Shi, Y.J. Liang, B. Zou, Appl. Catal. B 134 (2013) 293–301.
[48] J.J. Sun, X.Y. Li, Q.D. Zhao, M.O. Tadé, S.M. Liu, Appl. Catal., B 219 (2017) 259–268.
[49] J.R. Wang, F.E. Osterloh, J. Mater. Chem. A 2 (2014) 9405–9411.
[50] W. Zhao, Y. Liu, Z. Wei, S. Yang, H. He, C. Sun, Appl. Catal. B 185 (2016) 242–252.
[51] S. Paul, S. Ghosh, D. Barman, S.K. De, Appl. Catal. B 219 (2017) 287–300.
[52] X.Z. Liang, P. Wang, M.M. Li, Q.Q. Zhang, Z.Y. Wang, Y. Dai, X.Y. Zhang, Y.Y. Liu, M.H. Whangbo, B.B. Huang, Appl. Catal., B 220 (2018) 356–361.
[53] X.W. Li, W.D. Zhang, W. Cui, Y.J. Sun, G.M. Jiang, Y.X. Zhang, H.W. Huang, F. Dong, Appl. Catal. B 221 (2018) 482–489.
[54] S.B. Yang, D.B. Xu, B.Y. Chen, B.F. Luo, W.D. Shi, Appl. Catal. B 204 (2017) 602–610.
[55] X.C. Ma, Y. Dai, M. Guo, B.B. Huang, ChemPhysChem 13 (2012) 2304–2309.

[56] N.G. Miriam, P. Verma, Y. Kuwahara, T. Kamegawa, K. Mori, H. Yamashita, J. Photochem. Photobiol. A (2017) In Press.

[57] P. Verma, Y. Kuwahara, K. Mori, H. Yamashita, Catal. Sci. Technol. 7 (2017) 2551–2558.

[58] G.X. Yang, H.B. Yin, W.H. Liu, Y.P. Yang, Q. Zou, L.L. Luo, H.P. Li, Y.N. Huo, H.X. Li, Appl. Catal., B 224 (2018) 175–182.

[59] W. Zhao, Z. Wei, H. He, J. Xu, J. Li, S. Yang, C. Sun, Appl. Catal. A 501 (2015) 74–82.

[60] W. Zhao, Y. Guo, S. Wang, H. He, C. Sun, S. Yang, Appl. Catal. B 165 (2015) 335–343.

[61] W. Zhao, J. Li, Z. Wei, S. Wang, H. He, C. Sun, S. Yang, Appl. Catal. B 179 (2015) 9–20.

[62] S. Akhter, K. Allan, D. Buchanan, J.A. Cook, A. Campion, J.M. White, Appl. Surf. Sci. 35 (1988) 241–258.

[63] Q. Zhu, W.S. Wang, L. Lin, G.Q. Gao, H.L. Guo, H. Du, A.W. Xu, J. Phys. Chem. C 117 (2013) 5894–5900.

[64] V.K. Kaushik, J. Electron. Spectrosc. Relat. Phenom. 56 (1991) 273–277.

[65] X.H. Gao, S.F. Jiang, J. Li, D.H. Ding, S. Gao, G.D. Zheng, Chin. Sci. Bull. 39 (1994) 1066–1070.

[66] N. Martensson, P.A. Malmquist, S. Svensson, E. Basilier, J.J. Pireaux, U. Gelius, S.K. Nouveau, J. Chim. 1 (1977) 191–195.

[67] M. Ayyoob, M.S. Hegde, J. Chem, Soc. Faraday Trans. I 82 (1986) 1651–1662.

[68] S.Q. Liang, J. Zhou, X.L. Zhang, Y. Tang, G.Z. Fang, T. Chen, X.P. Tan, CrystEngComm 15 (2013) 9869–9873.

[69] D.K. Ma, M.L. Guan, S.S. Liu, Y.Q. Zhang, C.W. Zhang, Y.X. He, S.M. Huang, Dalton Trans. 41 (2012) 5581–5586.

[70] X.F. Zhou, C. Hu, X.X. Hu, T.W. Peng, J.H. Qu, J. Phys. Chem. C 114 (2010) 2746–2750.

[71] Y.Q. Yang, G.K. Zhang, S.J. Yu, X. Sheng, Chem. Eng. J. 162 (2010) 171–177.

[72] Y.Y. Li, J.S. Wang, H.C. Yao, L.Y. Dang, Z.J. Li, J. Mol. Catal. A: Chem. 334 (2011) 116–122.

[73] J. Kim, C.W. Lee, W. Choi, Environ. Sci. Technol. 44 (2010) 6849–6854.

[74] H.X. Fu, G.X. Lu, S.B. Li, J. Photochem, Photobiol. A-Chem. 114 (1998) 81–88.

[75] H.X. Fu, G.X. Lu, S.B. Li, Acta Phys.-Chim. Sin. 13 (1997) 106–112.

[76] H.X. Fu, G.X. Lu, S.B. Li, Toxico. Environ. Chem. 70 (1999) 333–347.

[77] H.X. Fu, G.X. Lu, S.B. Li, Adsorpt. Sci. Technol. 16 (1998) 117–126.

[78] H.F. Cheng, B.B. Huang, Y. Dai, X.Y. Qin, X.Y. Zhang, Langmuir 26 (2010) 6618–6624.